Three-dimensional structure of the Martian nightside ionosphere: Predicted rates of impact ionization from Mars Global Surveyor magnetometer and electron reflectometer measurements of precipitating electrons

Robert J. Lillis,[1] Matthew O. Fillingim,[1] and David A. Brain[2]

Received 6 July 2011; revised 19 September 2011; accepted 24 September 2011; published 13 December 2011.

[1] The nightside ionosphere of Mars is known to be highly variable: electron densities are below detection thresholds in certain regions and are almost comparable to the photoionization-produced dayside ionosphere in others. The factors controlling its structure include thermospheric densities, temperatures and winds, day-night plasma transport, plasma temperatures, current systems, meteoroid ablation, solar and galactic energetic particle events, and magnetic field geometry-topology and electron precipitation, none of which are adequately understood at present. Using a kinetic approach called Mars Monte Carlo Electron Transport, we model the dynamics of precipitating electrons on the nightside of Mars to study the impact of these last two listed factors (magnetic fields and electron precipitation) on ionospheric structure. As input, we use precipitating electron energy spectra and pitch angle distributions from the Mars Global Surveyor Magnetometer and Electron Reflectometer. We thus calculate ionization rate in three dimensions, both for specific observations and average cases. The very highest average rates are equivalent to photoionization rates on the dayside at high solar zenith angle. We predict complex geometrical patterns in the ionization and huge variability (~4 orders of magnitude) in peak ionization rates, both on single orbits and between the averages for different geographic regions, and find a bimodal distribution of predicted ionization rates where the highest rates correlate with the most vertical magnetic fields. This model can be used as input to electrodynamic models of the Mars ionosphere, which can be compared with, and informed by, data from the upcoming 2013 Mars Atmosphere and Volatile Evolution Mission.

Citation: Lillis, R. J., M. O. Fillingim, and D. A. Brain (2011), Three-dimensional structure of the Martian nightside ionosphere: Predicted rates of impact ionization from Mars Global Surveyor magnetometer and electron reflectometer measurements of precipitating electrons, *J. Geophys. Res.*, *116*, A12317, doi:10.1029/2011JA016982.

1. Introduction

1.1. Mars' Nightside Ionosphere

[2] The dayside ionosphere of Mars is primarily the result of photoionization of atmospheric neutrals by solar EUV flux, with a vertical structure and solar zenith angle (SZA) dependence that is described reasonably well by classical Chapman theory [*Chapman*, 1931a, 1931b]. Since 2001, more than two dozen publications on the Mars dayside ionosphere have appeared, primarily using data from the Radio Science (RS) experiment on Mars Global Surveyor (MGS) [*Tyler et al.*, 2001] and the Mars Advanced Radar for Surface and Ionospheric Sounding (MARSIS) on Mars Express [*Gurnett et al.*, 2005]. The variability of the dayside ionosphere is caused by solar EUV and X-ray variability, solar energetic particle (SEP) events, cosmic rays, neutral density variations, crustal magnetic fields and local plasma processes. *Withers* [2009] provides a comprehensive review of our current understanding of the dayside ionosphere

[3] In contrast, our understanding of the nightside ionosphere remains substantially incomplete, with comparatively little published data compared to the dayside. The nightside ionosphere does not start at solar zenith angle (SZA) = 90° because ionospheric altitudes (say, 100–200 km for the highest densities) are sunlit for SZA < ~105°–110°. Ionospheric plasma was only detected in 40% of Viking radio occultation profiles between SZA = 90° and 125° [*Zhang et al.*, 1990], of which the average peak electron density beyond 110° was 5×10^3 cm^{-3}, a factor of ~20–40 below subsolar values [*Gurnett et al.*, 2008]. Earth-Mars geometry prevents radio occultation measurements at SZAs above 125°.

[1]Space Sciences Laboratory, University of California, Berkeley, California, USA.
[2]Laboratory for Atmospheric and Space Physics, University of Colorado at Boulder, Boulder, Colorado, USA.

0148-0227/11/2011JA016982

Němec et al. [2010] conducted a comprehensive survey of MARSIS nightside observations up to SZA = 140° and found that ionospheric radar echoes were detected by MARSIS for SZA > 107° in only about 9% of cases, with a peak electron density detection threshold of 5–7 × 10^3 cm^3. Furthermore, for SZA > ~100°, *Gurnett et al.* [2008] reported "irregular patches" of ionosphere, with higher peak densities tending to occur in areas of strong crustal magnetic fields (note that the MARSIS Active Ionosphere Sounder is sensitive only to the top side ionosphere, i.e., above the peak). *Němec et al.* [2010] expanded upon this work, conducting a deep nightside survey of MARSIS airborne imaging spectrometer data, revealing 90 clear ionospheric echoes with SZA > 125°, none of which were found in regions of closed crustal magnetic field and for which higher peak electron densities were found where crustal fields were stronger.

[4] Also for SZA > 100°, *Safaeinili et al.* [2007] reported higher Total Electron Content (TEC) specifically where the crustal magnetic fields were closer to vertical than horizontal. *Lillis et al.* [2010b] showed that TEC for SZA > 110° can increase by more than a factor of 2 during a solar particle event. *Leblanc et al.* [2008] reported an example of a correlation between three simultaneous observations: increased TEC, increased precipitating electron flux and an observation of UV aurora on the nightside.

[5] This combination of low upper bound peak densities, irregularity and moderate correlation with crustal fields is consistent with some combination of electron impact ionization, transport from the dayside, dynamic magnetic field topology and possibly current systems, together controlling the nightside ionosphere. Oddly, there are no published nightside studies from either the MGS or Mars Express Radio Science experiments. Overall, the near-nightside ionosphere (107° < SZA < 140°) is highly variable and is not well understood, while the deep nightside ionosphere (SZA = 140°–180°) remains completely unexplored [*Withers*, 2009].

[6] The factors that control the spatial and temporal behavior of the nightside ionosphere are expected to be (1) neutral densities, temperatures, and structure therein (e.g., waves) [e.g., *Bougher et al.*, 1999; *Withers et al.*, 2003]; (2) thermospheric winds, which cause differential motion of electrons and ions and hence drive substantial currents [*Fillingim et al.*, 2010] though such currents have not yet been measured; (3) day-night plasma transport [e.g., *Uluşen and Linscott*, 2008; *Fränz et al.*, 2010]; (4) ablation by meteoroid influx, causing an ionization peak around 90 km [*Withers*, 2009]; (5) galactic cosmic rays (causing most ionization around 35 km [*Withers*, 2009]); (6) transient SEP events which cause ionization from the surface (greater than tens of MeV) up to ~150 km (tens of keV) [e.g., *Leblanc et al.*, 2002; *Luhmann et al.*, 2007]; (7) gamma ray burst events, which can cause massive ionization from 30 to 60 km in the terrestrial atmosphere [*Inan et al.*, 2007], corresponding to 0 to ~20 km on Mars [*Espley et al.*, 2008]; (8) magnetic field-aligned electrostatic potential drops, which may arise at and above ionospheric altitudes [e.g., *Dubinin et al.*, 2008a]; (9) recombination rates, which depend upon electron temperature [e.g., *Schunk and Nagy*, 2000]; (10) impact ionization by precipitating superthermal electrons from Mars' induced magnetosphere [e.g., *Nagy et al.*, 2004], and hence those electrons' energy spectra and pitch angle distributions (PADs) [e.g., *Brain et al.*, 2006]; and (11) magnetic field strength and topology, which varies with time because the often strong planet-fixed crustal magnetic fields reconnect with the draped and time-variable interplanetary magnetic field (IMF) as Mars rotates [e.g., *Halekas et al.*, 2006].

[7] Data remain sparse concerning factor 1 [e.g., *Withers*, 2006]. Factors 2–8 remain completely or almost unknown due to lack of reliable data. Factor 9 is also largely unknown because there exists only one measured profile of electron temperature [*Hanson and Mantas*, 1988], taken on the dayside, with no data below 200 km. It should be noted that the upcoming 2013 Mars Atmosphere and Volatile Evolution Mission (MAVEN) Mars Scout (http://lasp.colorado.edu/maven/) mission is slated to make many of these measurements. The work presented in this paper focuses on factors 10 and 11, i.e., how the energy and angular distributions of precipitating superthermal electrons and the properties of the magnetic fields that permeate the atmosphere and near-space environment combine to create complex structures of ionization in the nightside ionosphere.

1.2. Previous Modeling Efforts

[8] Several investigators have previously modeled electron transport through the Mars upper atmosphere. Such studies vary in approach from a simple analytic model [*Verigin et al.*, 1991], multistream models [*Haider et al.*, 1992; *Fox et al.*, 1993; *Fillingim et al.*, 2007; *Wedlund et al.*, 2011], a kinetic and fluid model [*Leblanc et al.*, 2006], to an analytic yield spectrum approach [*Haider*, 1997; *Seth et al.*, 2002; *Haider et al.*, 2002]. These models have been used to study ionization rates [*Haider et al.*, 2002; *Fillingim et al.*, 2007], auroral emissions [*Seth et al.*, 2002], atmospheric chemistry [*Haider*, 1997; *Haider et al.*, 2007] and expected Mars nightside ionospheric electron density profiles [e.g., *Fox et al.*, 1993]. The models have been used to examine the effects of different energy spectra of precipitating electrons under different atmospheric conditions, but to date have not included magnetic field gradients, nor anisotropic pitch angle distributions of the precipitating electrons.

[9] *Lillis et al.* [2009] used the kinetic MarMCET (Mars Monte Carlo Electron Transport) model to account for pitch angle anisotropies and magnetic field gradients. They showed that the sensitivity of peak ionization rates to pitch angle anisotropy increases strongly with crustal magnetic field gradient. In other words, if the crustal gradient is strong, different PADs result in very different ionization profiles, whereas weak crustal gradients results in very similar profiles regardless of PAD. This is because precipitating electrons with initial pitch angles close to 0° or 180° (i.e., field-aligned velocities) are almost unaffected by the crustal fields whereas those with initial pitch angles closer to 90° (i.e., velocities more perpendicular to the field) feel the mirror force more strongly and may magnetically reflect before causing any ionization [*Lillis et al.*, 2004, *Lillis et al.*, 2008]. Therefore these two considerations must be taken into account for accurate representation of impact ionization in strong crustal field regions. As a corollary, isotropic PADs result in very similar ionization rate profiles (~20% difference) regardless of crustal gradient strength [*Lillis et al.*, 2009].

1.3. Three-Dimensional Structure of Nightside Ionization

[10] As mentioned above, the sparsely explored nightside ionosphere appears to be highly irregular and somewhat correlated with crustal field strength and magnetic elevation angle, with peak electron densities most of the time below 5×10^3 cm^{-3}. The purpose of this paper is to investigate the expected range of three-dimensional ionization structures. Both of the important determining factors, i.e., the crustal magnetic fields and the angular and energy distribution of the precipitating electrons, have been explored by the MGS magnetometer and electron reflectometer (MAG/ER) experiment [e.g., *Mitchell et al.*, 2001; *Lillis et al.*, 2004; *Brain et al.*, 2007] and the Mars Express Analyzer of Space Plasmas and Energetic Atoms 3 experiment [e.g., *Barabash et al.*, 2007; *Dubinin et al.*, 2009]. Therefore the pieces are in place to conduct a modeling study that incorporates realistic electron energy spectra, pitch angle distributions, magnetic field geometries and neutral density profiles.

[11] We use data from MAG/ER because its magnetometer allows determination of electron pitch angles and the near-circular orbit (i.e., approximately constant altitude) of MGS allows relatively straightforward comparison between geographic locations. We concentrate on the Terra Sirenum–Terra Cimmeria region in the southern hemisphere (20°–70°S, 140°–220°E) where the crustal fields are strongest. We present case studies of the expected ionization patterns caused by the precipitation of electrons measured by MAG/ER on three sample orbits of MGS in early June 2001 (0200 LT, just before northern autumnal equinox at L_s = 172°). In addition, we show maps and profiles of the "average" nightside ionization over the course of the MGS mission. We also examine some limited ionization statistics.

[12] Finally, though it is trivial to "convert" ionization rate to electron density by assuming photochemical equilibrium, a single O_2^+ recombination rate [e.g., *Sheehan and St.-Maurice,* 2004] and Viking dayside electron temperature profile [e.g., *Chen et al.*, 1978; *Hanson and Mantas*, 1988], as was done by *Lillis et al.* [2009], we choose not to do so in this paper (at least not for the figures) because any such derived electron densities are probably highly inaccurate. This is because we have no information, other than the two dayside Viking descent profiles [*Nier and McElroy*, 1977], about the relative fractions of different atmospheric gases at different altitudes on the nightside, nor about the electron temperature profile on the nightside. Further, we have no idea of the effect of day-night plasma transport or vertical plasma diffusion, nor curvature or gradient plasma drifts nor wind-driven currents all of which will alter electron density structures, and which will be substantially complicated by the strong and spatially inhomogeneous crustal magnetic fields in this region. Therefore, we shall limit ourselves to examining ionization rate, a very important quantity and one about which we can be at least reasonably confident.

2. Method

2.1. Mars Monte Carlo Electronic Transport (MarMCET) Model

[13] MarMCET takes a kinetic Monte Carlo approach to electron motion in a planetary atmosphere and is described in detail by *Lillis et al.* [2008, sections 3–5] and, specifically for the purpose of calculating ionization, by *Lillis et al.* [2009, section 2.1]. It takes as input the following variables: (1) starting altitude, energy and pitch angle of a single downward traveling electron; (2) the path, in three dimensions, of the magnetic field line to which the electron is bound, also known as the electron's guiding center path; (3) as a function of distance along a given magnetic field line, magnetic field magnitude (the individual components already define the field line itself) and density of the desired neutral species (O, O_2, N_2, CO_2, CO, and Ar can be included); and (4) cross sections for electron-neutral collisions, including elastic collisions, dissociation, excitation, ionization, angle dependence and differential cross sections for this secondary electron emission.

[14] The output of MarMCET, for our purposes, is a list of ionizations and their altitudes caused by each primary electron. For every neutral density and magnetic field configuration in this paper, 10,000 electrons are run for each of 20 logarithmically spaced energies from 15 eV to 20 keV and for 12 equally spaced downward traveling pitch angle bins between 0 and $\pi/2$, totaling 2.4 million electrons. The minimum necessary number of electrons was found to be 8000–10,000, above which the calculated ionization profile did not change noticeably. Electrons below ~15 eV were not considered because they do not cause ionization while 20 keV is the upper end of the energy range of the MGS ER instrument. Simulations do not have to be run separately for different input energy spectra or PADs, since the contributions from each energy-pitch angle can be summed and weighted accordingly to predict the ionization rate profile for a given energy spectrum and PAD [*Lillis et al.*, 2009]. While measurements cover the relevant energy range for ionization (10 eV–20 keV), PAD coverage does not always extend between 0° and 90° (where 0° is assumed to be downward along the magnetic field line). Therefore we assume the flux at all unsampled pitch angles is equal to the most field-aligned pitch angle bin for which data exists (see Figure 5d for an example of this extrapolation). It should be pointed out that data always exist for pitch angles from 83° to 97° due to the ±7° aperture of the MGS ER instrument. How close to 0° (or 180°) the pitch angle sampling extends is determined by how close to 90° is the angle between the instrument axis and the local magnetic field [e.g., *Mitchell et al.*, 2001].

2.2. Magnetic Field Model Used

[15] For the three-dimensional magnetic field used by MarMCET, we use a vector sum of internal and external magnetic fields. The internal magnetic field is a spherical harmonic representation of a model of the crustal magnetic field calculated using a correlative technique on the 7 years (1999–2006) of nightside mapping orbit observations from the MGS magnetometer. Field components of internal and external origin are separated using techniques developed by *Purucker* [2008]. The model is explained in detail by *Lillis et al.* [2010a, Appendix A] and has somewhat lower noise than previous models, although we note that the precise choice of magnetic field model is not very important because

the region in question (Terra Cimmeria) has such strong fields that most models [e.g., *Cain et al.*, 2003; *Arkani-Hamed*, 2002; *Langlais et al.*, 2004; *Whaler and Purucker*, 2005] give similar results.

[16] The constant external field is calculated in 2 different ways. For the average nightside ionosphere (section 3.2), the (x, y, z) components of the external field are (−12.0, 1.0, 1.5) nT in MSO coordinates (MSO stands for Mars Solar Orbital, where **x** points from the center of Mars toward the sun, **y** points in the direction of Mars' orbital motion and **z** completes the right-hand system). This is a typical tail-lobe magnetic field appropriate for 0200 LT. This tail-lobe field has a bimodal distribution of approximately sunward and antisunward magnetic fields, depending on the direction of the Interplanetary Magnetic Field (IMF) and a magnitude between 5 and 25 nT, depending on solar wind pressure [*Ferguson et al.*, 2005]. For the case study of individual orbital passes (section 3.1), the constant external field is taken to be the difference between the total field measured at the spacecraft location and the internal field model evaluated at that same location.

[17] The orientation of the planet-fixed crustal fields in MSO coordinates are determined by the local time (we choose 0200 LT, where all MGS nightside data are approximately collected) and the season (we choose L_s = 172° corresponding to our case study data in June 2001, giving a subsolar latitude of 3°N).

[18] Starting at each point on a 1° × 1° grid at the MGS mapping orbit altitude (370–390 km) in the region between 70°S and 20°S and 140°E and 220°E (50° × 80° = 4000 points), we follow the field lines down to an altitude of 70 km, recording the latitude, longitude, altitude and magnetic field magnitude of each point in a 400 element array, resulting in (400 × 4000) 1.6 million grid points. In this region, crustal magnetic field magnitude is everywhere >50 nT at the MGS altitude of 400 km, and increases exponentially with decreasing altitude, reaching ~1500 nT around 100 km. Therefore, we can safely ignore small to moderate magnetic field perturbations at the boundaries of open and closed magnetic topologies, the largest of which occur where we observe an accelerated downward traveling electron population. The perturbations have magnitudes of typically <20 nT [*Brain et al.*, 2007]. These perturbations are seen in Figures 2a–4a as small "notches" in the magnetic elevation angle.

2.3. Neutral Density Model Used

[19] We use predictions from the Mars Climate Database version 4.3 [*Millour et al.*, 2008], which come directly from a large ensemble of simulation runs of the Laboratoire de Météorologie et Dynamique (LMD) Mars Global Circulation Model (MGCM). The LMD-MGCM model is a physics-based model of the Martian atmosphere from the ground up to the lower exosphere [*Forget et al.*, 1999, 2009; *Angelats i Coll et al.*, 2004]. We take predictions for neutral densities of O, N_2, CO_2, and CO (the neutral species simulated by the LMD-MGCM) for each of our 1.6 million grid points (i.e., predictions for each location in three dimensions) for the same local time (0200 LT), season (L_s = 172°), dust scenario (Mars year 24) and solar UV flux (solar maximum) as our case study data of June 2001.

3. Modeling Results

3.1. Case Study: Ionization Caused by Measured Precipitating Electrons

3.1.1. Three Typical Orbital Passes

[20] It is instructive to examine the expected patterns of ionization resulting from typical nightside angular and energy distributions of precipitating electrons measured by the MGS MAG/ER experiment. We define nightside to be locations where the solar zenith angle (SZA) is greater than 117° (i.e., where all altitudes below 415 km are in darkness). Three representative nightside passes over the Terra Cimmeria region are shown in Figures 1–4. In all cases the spacecraft is moving south with south latitude increasing from 20° to 64°, SZA decreasing from 140° to 117° and altitude decreasing from ~385 to ~370 km. Figure 1 shows the predicted three-dimensional ionization rate resulting only from the electron energy-angle distributions measured by the MGS MAG/ER experiment on these three passes, forming curtains of ionization as the electrons travel along magnetic field lines. Figures 2a–4a show the SZA and magnetic elevation angle. Figures 2b–4b show the flux in the 95–148 eV energy channel as a function of pitch angle, normalized for each PAD. As mentioned earlier, pitch angle coverage varies as the angle varies between the magnetic field vector and axis of the MGS ER electrostatic analyzer (whose field of view spans only 360° × 14° [*Mitchell et al.*, 2001]). Figures 2c–4c show energy-latitude spectrograms of the downward traveling electron flux. Figures 2d–4d plot the logarithm of the ionization rate projected on a plane defined by radial lines intersecting the spacecraft trajectory, i.e., a "side view" of the ionization rates. The white space in Figures 2d–4d has no meaning in the sense that none of the electrons we measure can reach those regions in our simulation; there could be trapped electron populations causing ionization in those regions but we cannot measure them.

[21] Note that PADs are essentially meaningless when the flux levels are so low that we are seeing mostly residual background counts. This is the case over substantial parts of all 3 tracks shown (examples include track 1, latitudes −33° to −38° and −42° to −48°, and track 2, latitudes −23° to −37°). Note also that, although there are places where field lines are closed loops attached to the crust at both ends, we only trace the magnetic field lines from the spacecraft location downward toward the planet and consider only the downward traveling portion of the electron flux.

3.1.2. Effect of Magnetic Topology and Pitch Angle Distributions on Ionization

[22] Magnetic topology refers to the "connectedness" of a given magnetic field line, i.e., to what it is connected. If it is connected to the planet at one end and the Interplanetary Magnetic Field (IMF) at the other end, it is an "open" topology (e.g., at the Earth's magnetic poles). If it is connected to the planet at both ends, it is a "closed" topology (e.g., the Earth's equatorial regions). Since electrons below a few keV have small gyroradii (e.g., 10.7 km for a 1 keV electron in a 10 nT magnetic field; lower energies or stronger

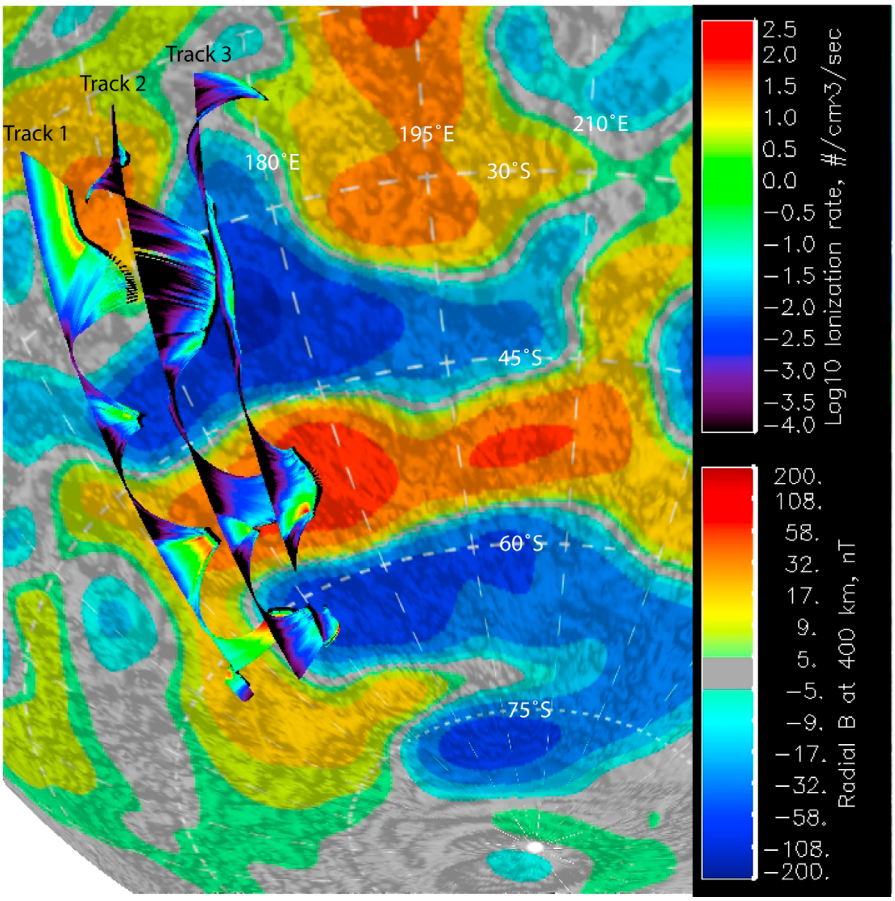

Figure 1. The predicted three-dimensional ionization rate for three separate Mars Global Surveyor (MGS) orbital passes. The rainbow colors (upper color scale) plot the ionization rate resulting only from the electron energy-angle distributions measured by the MGS magnetometer and electron reflectometer (MAG/ER) experiment on these three passes, forming "curtains" of ionization as the electrons travel along magnetic field lines. The planetary sphere beneath is shaded by topography and colored according to the radial component of the crustal magnetic field at 400 km (lower color scale). Track 1 covers the time range 4 June 2001, 1006:53–1020:51 UT and is examined in Figure 2. Track 2 covers 1 June 2001, 0731:20–0745:43 UT and is examined in Figure 3. Track 3 covers 5 June 2001, 0940:11–0954:03 UT and is examined in Figure 4.

fields result in smaller gyroradii), they are essentially bound to move along (and not across) field lines and since those electrons ionize atmospheric neutrals, magnetic topology plays an important role in electron impact ionization.

[23] As shown in Figures 2–4, the measured magnetic field vector rotates about the east–west direction more than 360° as the spacecraft passes through regions where the crustal field is alternately radially upward, predominantly horizontal and radially downward. This crustal field structure interacts with the dynamic Martian magnetotail, resulting in both open and closed magnetic topologies occurring several times on each pass. Magnetic topology is typically indicated by electron PADs [*Lillis et al.*, 2008; *Brain et al.*, 2007] and we see examples of several types of PAD during these three passes, resulting in a wide range of ionization rate profiles.

[24] One-sided loss cones (e.g., track 1, −27° latitude; track 2, −52°; track 3, −53°) imply open magnetic field lines, where solar wind electrons can precipitate into the Martian atmosphere. We also see apparently double-sided, somewhat field-aligned PADs in track 1, −51° to −55° and −30° to −33°, for which the best explanation is open topology and a one-sided loss cone between 155° and 180°, beyond our pitch angle coverage (because closed topology must result in flux depletion closer to 0° and 180°). Wherever we see open topology, we see substantial downward traveling electron flux and peak ionization rates from in the range 5–220 cm^{-3} s^{-1}. In general, these one-sided loss cones occur more frequently for higher elevation angles [*Brain et al.*, 2007, Figure 7], which is consistent with these three orbital passes where most occur when the magnetic elevation angle is >±40°.

[25] Double-sided loss cones (e.g., track 1, −56° latitude; track 2, −39° latitude; track 3, −37° latitude) imply closed magnetic field lines (i.e., attached at both ends to the crust), on which bound electrons magnetically mirror repeatedly. These can occur for any magnetic elevation angle, though they are much more common for horizontal magnetic field [*Brain et al.*, 2007]. Double-sided conics (e.g., track 1, −34° latitude) also imply closed field lines and resemble

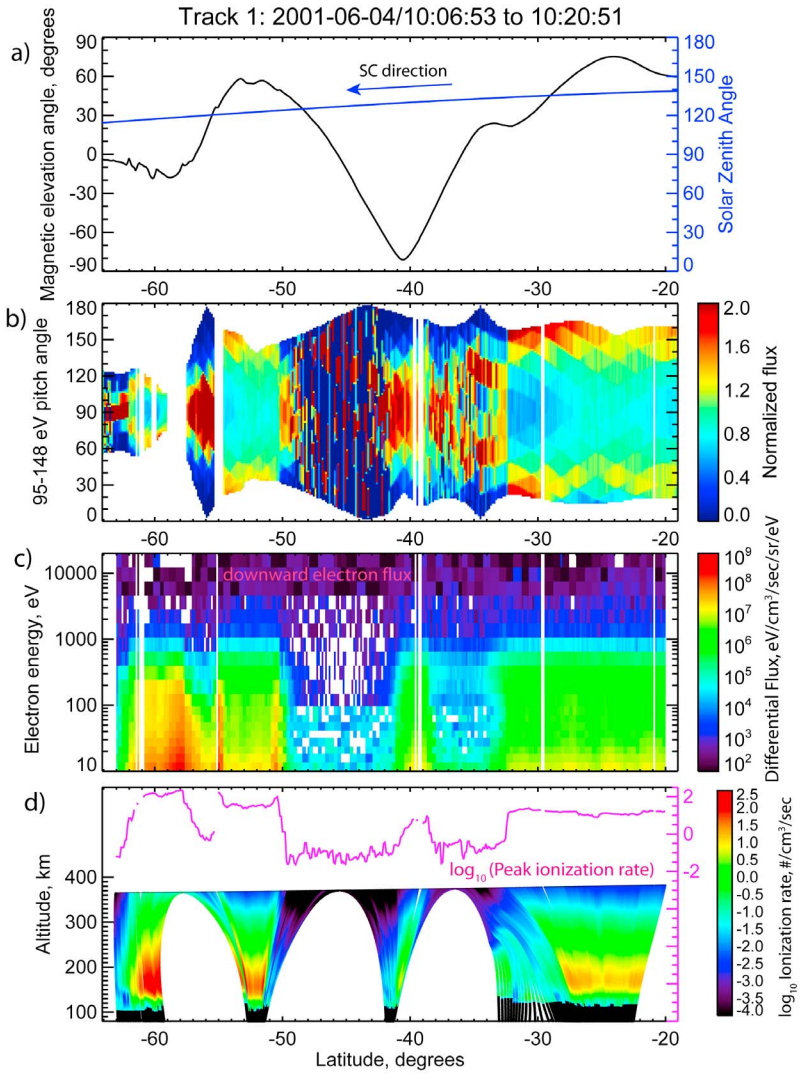

Figure 2. Relationship between magnetic field, precipitating electrons, and ionization profiles, shown as a function of latitude for a single MGS orbital pass in June 2001. (a) Solar zenith angle and magnetic field elevation angle. (b) Normalized pitch angle distribution at 107 eV. (c) Differential energy flux spectrum of the downward traveling portion of the electron distribution. (d) Individual magnetic field lines traced from the spacecraft down to 80 km and projected into a plane, colored according to ionization rate and the base-10 logarithm of the peak ionization rate plotted as a function of the spacecraft latitude (not latitude at the peak).

two-sided loss cones which have been depleted near 90° pitch angle [*Brain et al.*, 2007; *Ulusen et al.*, 2011], perhaps by time-variable parallel electric fields or heating by a variety of wave mechanisms [*Eliasson et al.*, 1996]. On these three passes, we typically see slightly lower downward fluxes for closed topologies compared with open topologies, but in fact we see proportionally much lower ionization because such "trapped" PADs cause far less ionization than isotropic PADs. The reason is that, in regions of strong crustal magnetic field such as these, electrons with pitch angles near 90° magnetically reflect before they can cause any substantial ionization, whereas field aligned electrons penetrate much deeper into the atmosphere [*Lillis et al.*, 2009]. An alternate way to express this is that, by definition, a trapped PAD consists predominantly of electrons that have not been absorbed by the atmosphere or scattered off the field line on previous bounces. Therefore, when calculating the electrons' "next" interaction with the atmosphere one expects to see a relatively small effect.

[26] We see some clear examples of trapped PADs causing little or no ionization. First, on track 1, −55° latitude, the magnetic topology abruptly changes from open to closed as the spacecraft travels south. Despite the downward traveling electron energy spectrum not changing substantially, the peak ionization rate falls nearly 3 orders of magnitude from 175 to 0.4 cm^{-3} s^{-1}. Next, on track 2, the flux spikes at −39° and −53° are trapped distributions and the peak ionization rate barely rises above the background, whereas the (albeit larger) spike at −52° shows a clear increase in peak rate. Similarly on track 3, the trapped precipitating electron

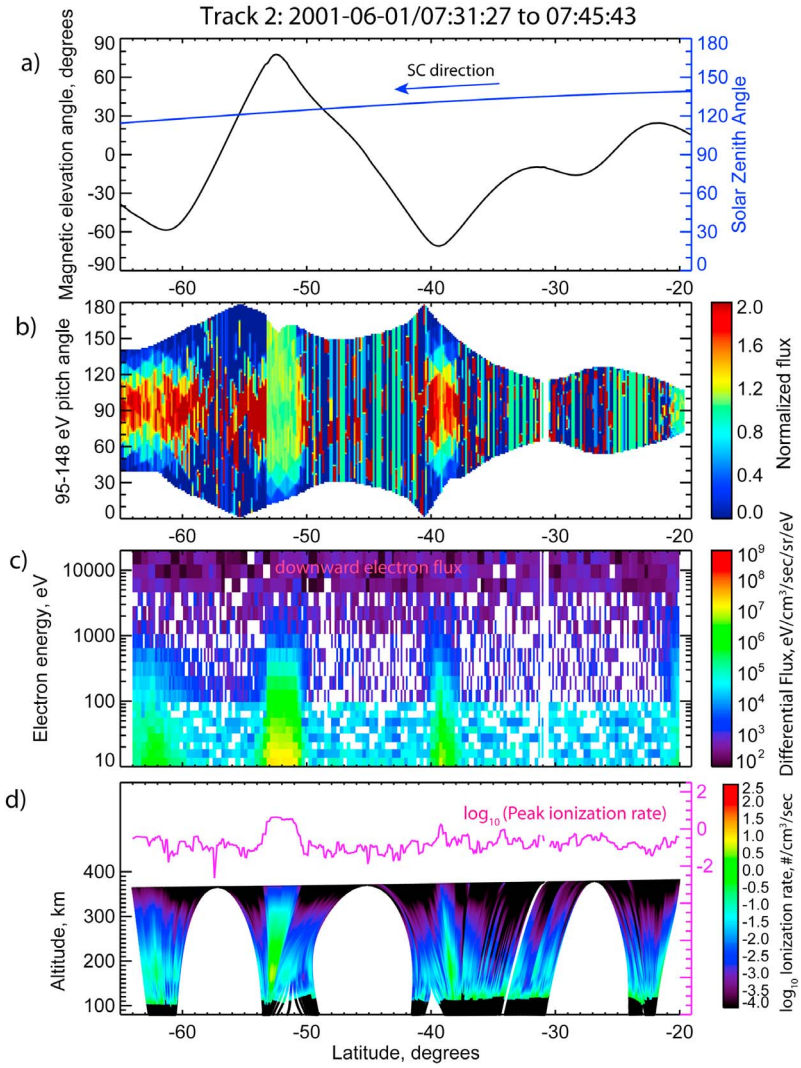

Figure 3. Same as Figure 2 but for track 2.

distributions seen from −28° to −38° cause very modest ionization whereas the isotropic distributions at −54° and −64° cause peak ionization rates to jump up over 150 cm^{-3} s^{-1}, comparable to the photo-produced dayside ionospheric.

[27] Last among topologies, we see plasma voids, where there is no detectable electron flux (above instrument background) at any energy or pitch angle (e.g., track 1, −33° to −38°; track 2, −20° to −37°), which are also indicative of closed field lines since open field lines always contain some solar wind plasma. These distributions result in very low ionization rates.

[28] We also observe very rapid changes in ionization rate in "cusp" regions, where topology switches rapidly from open to closed or vice versa. For example, in track 1, we see sharp transitions at −33°, −50° and −55° latitude. Such transitions are sometimes accompanied by localized increases in the downward traveling electron flux (seen at −50° and −55° latitude on track 1). These narrow currents are accompanied by perturbations in the magnetic field on length scales too short to be due to variations in the crustal field [*Brain et al.*, 2006; *Halekas et al.*, 2006].

3.2. Average Nightside Ionosphere

[29] Having examined typical predicted ionization rate profiles for individual orbits, we now investigate the average three-dimensional pattern of nightside ionization, resulting from typical geographic variability in the precipitating energy spectrum, the PADs and the neutral atmosphere. Given the intrinsic variability of electron precipitation in near-Mars space [e.g., *Dubinin et al.*, 2008b; *Brain*, 2006], and because all the MGS MAG/ER is at 0200 LT, we do not expect any particular snapshot to look like this average situation, but it is nonetheless instructive to put together a three-dimensional average "picture" of Martian nightside ionization. *Dubinin et al.* [2008b] examined geographic patterns of omnidirectional 30–80 eV electrons on the nightside from MAG/ER. We shall go further by isolating the average downward traveling portion of the electron population (i.e., the portion relevant for ionization), across all energies sampled by the MAG/ER instrument, as well as its pitch angle distribution, and predicting the resulting average three-dimensional ionization pattern.

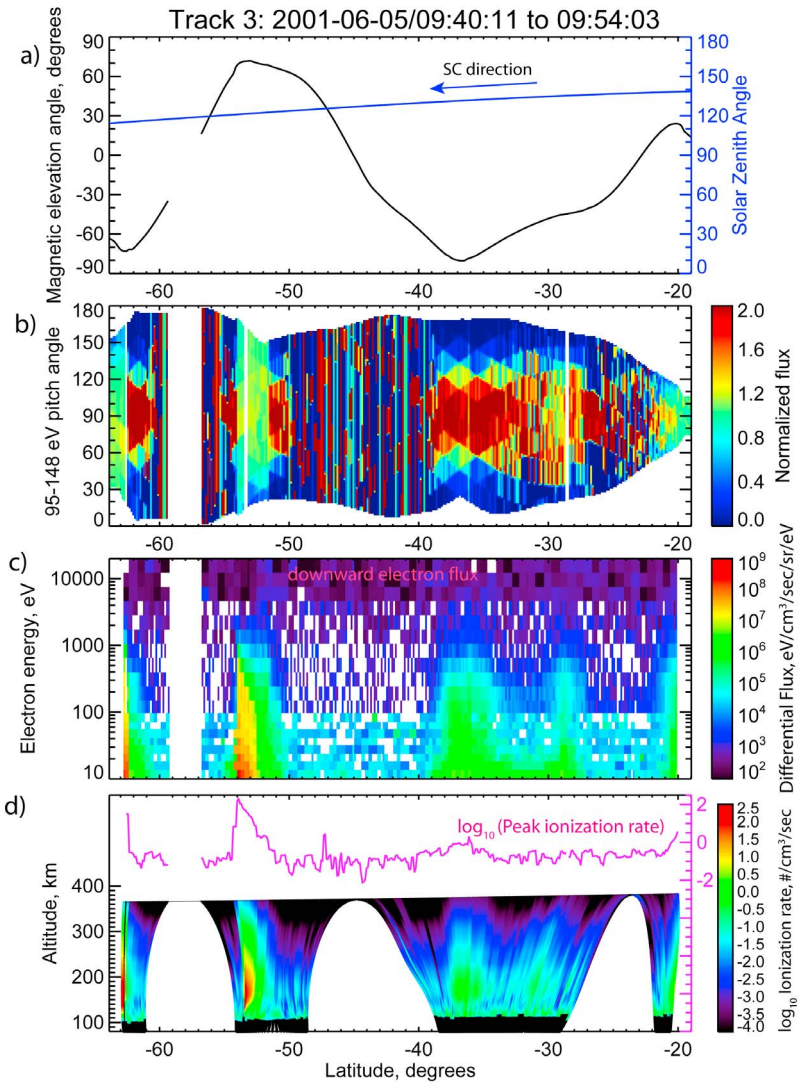

Figure 4. Same as Figure 2 but for track 3.

[30] For each of the aforementioned 4000 individual 1° × 1° pixels, we calculated the average energy spectra and PADs of downward traveling electrons over the entire MGS mapping orbit mission (May 1999–November 2006). These two-dimensional energy-angle flux distributions spanned the 19 logarithmically spaced energy channels (over the range 10 eV–20 keV) intrinsic to the MGS ER PAD data [*Mitchell et al.*, 2001] and were resampled from the variable instrumental pitch angle bins (pitch angle bins vary as the angle varies between the magnetic field direction and the instrument axis) to nine equal pitch angle bins spanning 0°–90°, where 0° is taken to be downward toward the planet along the magnetic field line.

[31] We use the magnetic field geometry described in section 2.2 (i.e., the vector sum of a crustal field model and a typical tail-lobe field) and the neutral density profile described in section 2.3 (i.e., LMD MGCM predictions for the same local time, season, dust opacity, solar activity and geographic location as our case study of early June 2001). With these inputs, we follow our downward traveling electron energy-angle distributions along the magnetic field lines from MGS spacecraft altitude into the atmosphere using MarMCET and calculate the average ionization rate along each field line, thereby constructing a three-dimensional picture of Martian nightside ionization in this region of strong crustal magnetic fields.

[32] It is difficult to capture in sufficient detail in one figure the average three-dimensional structure of the ionization as well as the factors that determine that structure: magnetic field strength and geometry, neutral density profile and electron spectrum and PAD. Therefore we choose to show 4 complementary figures.

3.2.1. Individual Profiles

[33] Figure 5 examines five sample locations within this 50° × 80° patch of Mars, showing the assumed magnetic field magnitude, magnetic elevation angle and mass density for that location, plus the pitch angle distributions (at 107 eV, an energy bin where count rates are typically sufficient to ensure pitch angle statistics are reliable) and average measured precipitating energy spectrum (averaged

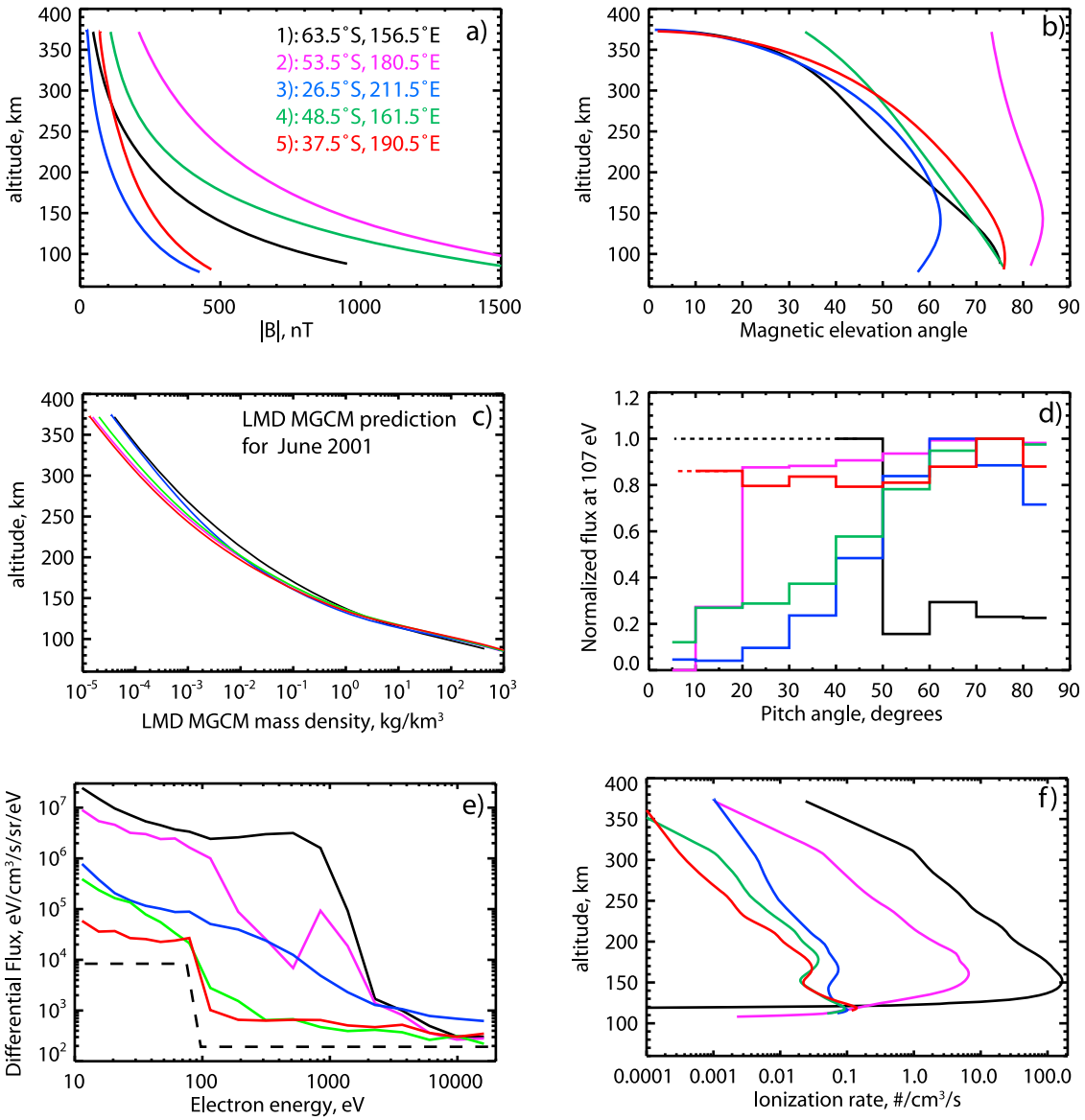

Figure 5. For five sample locations within the "average" nightside ionization map, we plot (a) the magnetic field profile; (b) the magnetic elevation angle profile; (c) the assumed neutral mass density profile; (d) the average measured electron pitch angle distribution at 107 eV, where dotted lines represent the assumed continuation of instrument-truncated PADs; (e) the average measured downward traveling differential energy flux spectrum, where the dashed line represents average instrument background for these five pixels; and (f) the resulting ionization rate profiles calculated by Mars Monte Carlo Electron Transport (MarMCET).

over all downward traveling pitch angles). Figure 5f shows the resulting ionization rate profiles for these sample locations.

[34] First, we see variations of factors of 2–3 in the LMD MGCM-predicted neutral density profiles at the altitudes of greatest ionospheric interest (120–250 km). These have a minor effect on the resulting ionization profiles, in the sense of moving them upward-downward by a few kilometers. However, we see great differences in magnetic field strength and geometry, as well as a wide range of electron pitch angle and energy distributions. These result in variations in average ionization rate of more than 3 orders of magnitude, just among these examples.

[35] For instance, the black lines represent pixel 1, an area of moderate crustal magnetic field strength but very high precipitating fluxes, where we assume a field aligned PAD due to limited PAD coverage and where the electron spectrum typically has a nonnegative slope between ~100 and ~600 eV, a telltale sign of acceleration of solar wind electrons [*Brain et al.*, 2006]. Indeed, *Halekas et al.* [2008] showed that this region (~155°E, 63°S) is an area commonly displaying such accelerated electron spectra. The result is a

very high ionization rate, peaking at ~165 s^{-1} cm^{-3} (seventh highest out of the 4000 pixels; the highest was 453 s^{-1} cm^{-3}). Assuming the same reasonable recombination rate profile used by *Lillis et al.*, 2009, Figure 2d], based on O_2^+ recombination and the Viking-based model electron temperature profile of *Chen et al.* [1978], this would correspond to a peak electron density of 2.9×10^4 cm^3 (the highest was 4.5×10^4 cm^3) which is comparable to dayside photo-peak densities seen at solar zenith angles >85° [*Withers*, 2009; *Gurnett et al.*, 2005].

[36] The pink lines represent pixel 2, among the strongest crustal magnetic fields on the planet at 180°E, 53°S, where the topology is open only ~30% of the time [*Brain et al.*, 2007]. The weaker average precipitating spectrum combined with the trapped PAD results in substantially less ionization compared with the black line. The peak at 1 keV in the spectrum is the result of a small number of averaged spectra containing an accelerated population.

[37] The blue and green lines represent pixels 3 and 4, in comparatively weak and very strong crustal magnetic field regions with similar average PADs and neutral density profiles, respectively. However, pixel 3 receives higher precipitating electron flux on average and therefore has a higher ionization rate at all altitudes. Last, pixel 5 is typically a plasma void, where precipitating fluxes are not much higher than background levels and ionization rates are consequently very low. All the averaged energy spectra have very low fluxes above a few keV, giving similar, low ionization rates of ~0.1 cm^{-3} s^{-1} around ~120 km.

3.2.2. Patterns of Downward Traveling Electron Flux

[38] Figure 6 shows maps of average electron flux at 4 energies (35 eV, 107 eV, 463 eV, 2 keV) averaged over all downward traveling pitch angle bins, and maps of the resulting ionization rate at the average altitudes of greatest ionization (for our assumed atmosphere) for each energy, along with contours of radial magnetic field. For example, 107 eV electrons cause greatest ionization around 150 km. We can clearly see from the left column that the magnetic topology affects the average flux of precipitating electrons as there are substantial "pockets" (totaling approximately 20% of the examined area) with little or no precipitation on average. However, more than this, the convergence of the magnetic field (as the electrons travel downward toward the planet) concentrates the ionization into localized regions where the magnetic field is most radial. Figure 6 (right) shows that the area of these regions decreases with decreasing altitude. Just as in the case of the individual orbital passes, the open and closed magnetic field topology causes sharp boundaries between areas of strong ionization and areas of no ionization. Given the small gyroradii (approximately a few kilometers) of the precipitating electrons, this is likely to result in currents driven by strong plasma pressure gradients, as examined by *Fillingim et al.* [2010].

3.2.3. Average Three-Dimensional Pattern of Ionization

[39] Figure 7 plots the average predicted ionization rate in 3 dimensions, traced from the middle of every 1° × 1° pixel at MGS spacecraft altitude, along the assumed magnetic field line, down to an altitude of 80 km. The dark and light green colors on the globe represent the radial component of the crustal magnetic field measured by MGS at 400 km. For clarity, Figure 7 (top) shows only those points below 200 km altitude, while Figure 7 (bottom) shows all points. Animations 1 and 2 contain an extension of Figure 7: 31-frame movies (animated GIFs) showing the three-dimensional ionization rates up to and including 80 km, 90 km, 100 km, …, 380 km.[1] The color scales are the same for the static Figure 7 and Animations 1 and 2.

[40] Figure 7 most clearly shows how particle precipitation interacts with magnetic geometry and topology in order to create complex patterns of ionization. Some patterns are linear, like the "triple junction" centered at 37°S, 174°E or the "main stripe" centered at 52°S, 180°E. Others form what resemble point source "fountains," like that seen at 23°S, 152°E. Note also several places with very high average rates of ionization, such as the long, curved feature of mostly red (in Figure 7, top), starting near 70°S, 150°E and continuing north and eventually east with only a small break near 55°S.

3.2.4. Correlation With Magnetic Elevation Angle

[41] It is clear from the preceding figures and discussion that higher ionization rates are to be expected in areas of open magnetic topology, which are closely correlated with areas where the magnetic field at MGS altitude is more vertical [*Brain et al.*, 2007]. To examine this quantitatively, Figure 8 shows the peak ionization rate as a function of elevation angle and a histogram of peak ionization divided into measurements where the magnetic elevation angle is less than/greater than 45°. It is clear from Figure 8 that there appears to be a bimodal distribution of ionization rates in this region. This is likely due to the dichotomy between "mostly open" field topologies where we often see higher precipitating fluxes, and "mostly closed" magnetic field topologies where we usually see very low fluxes. The former areas typically have more vertical magnetic field lines (elevation angles >45°) and the latter typically have more horizontal field lines (elevation angles <45°).

4. Discussion and Conclusions

4.1. Limitations and Uses of This Exercise

[42] The complex, modeled patterns of electron impact ionization shown in the earlier figures are obviously incomplete: they are merely an average of a subset (0200 LT) of those which we expect to find in reality on the nightside of Mars. Further, while our calculations used as input the downward electron fluxes on a complete surface at ~400 km and therefore capture all ionization caused by precipitating electrons on open field lines (within our geographic box), there are undoubtedly unsampled closed field lines below this surface, which may contain trapped distributions of solar wind electrons. Therefore, the "bands" of ionization are likely not quite as narrow as they appear in Figures 1, 6, and 7. These solar wind electrons were likely acquired through pitch angle scattering or reconnection as the fixed crustal fields rotate with respect to the draped induced solar wind interaction magnetic field [*Brain et al.*, 2007; *Ulusen et al.*, 2011] which cause ionization. As the IMF direction and subsolar latitude vary throughout the year, we can expect substantial variability in exactly which closed field lines acquire superthermal electrons. Therefore the ionization regions will likely expand, contract and change shape as these external variations occur.

[43] Further, the model of the crustal magnetic field we used [*Purucker*, 2008; *Lillis et al.*, 2010b] is only as good as the MGS MAG data from which it was constructed, which is

[1] Animations are available in the HTML.

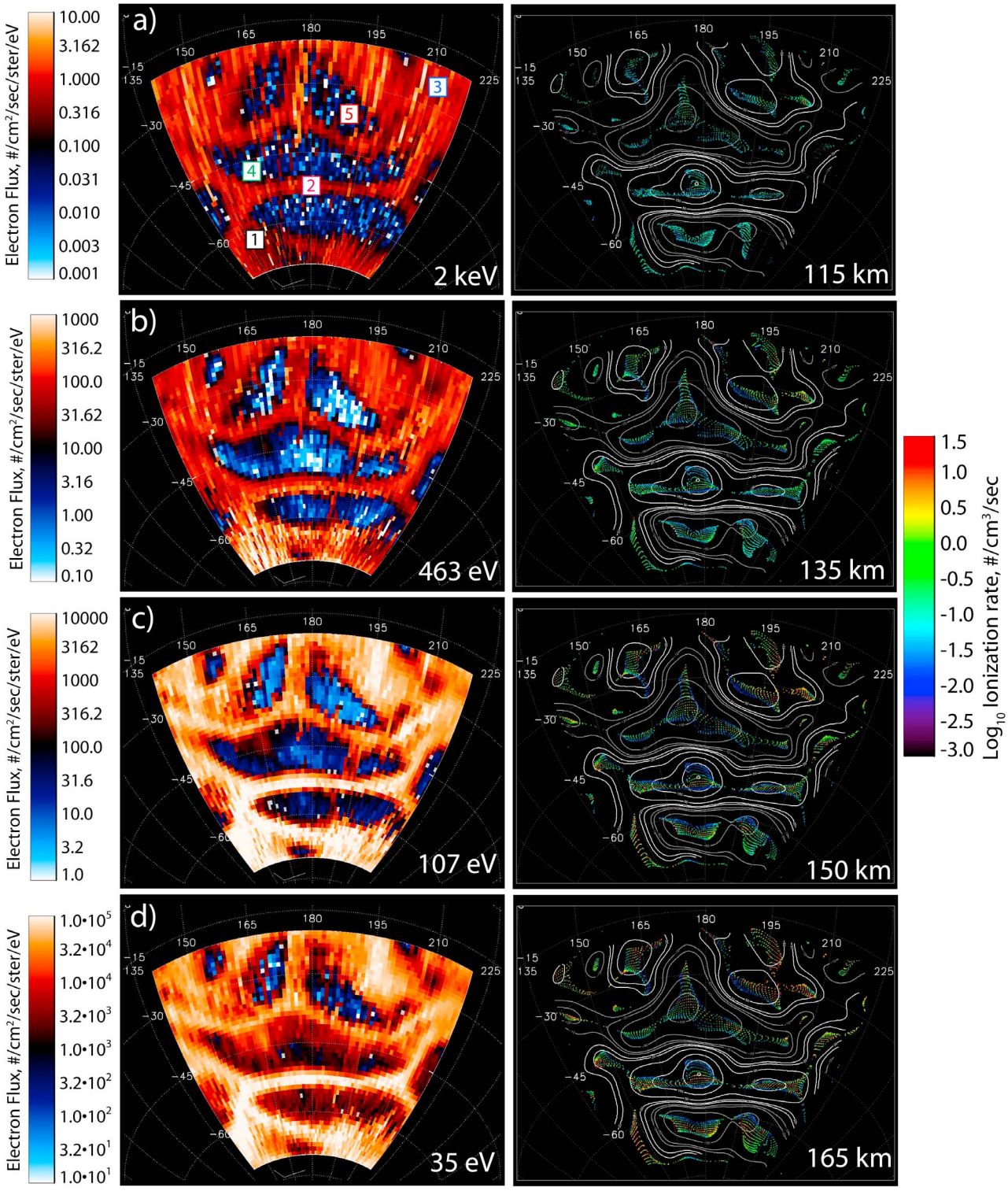

Figure 6. (left) Average downward traveling flux of electrons at each of four different superthermal energies as a function of geographic location, averaged over the entire mapping phase of the MGS mission (May 1999–November 2006). (right) Resulting ionization rate at the altitudes where those energies cause maximum ionization. Readers are encouraged to enlarge the right-hand column to clearly observe how the ionization rate varies and where ionization occurs.

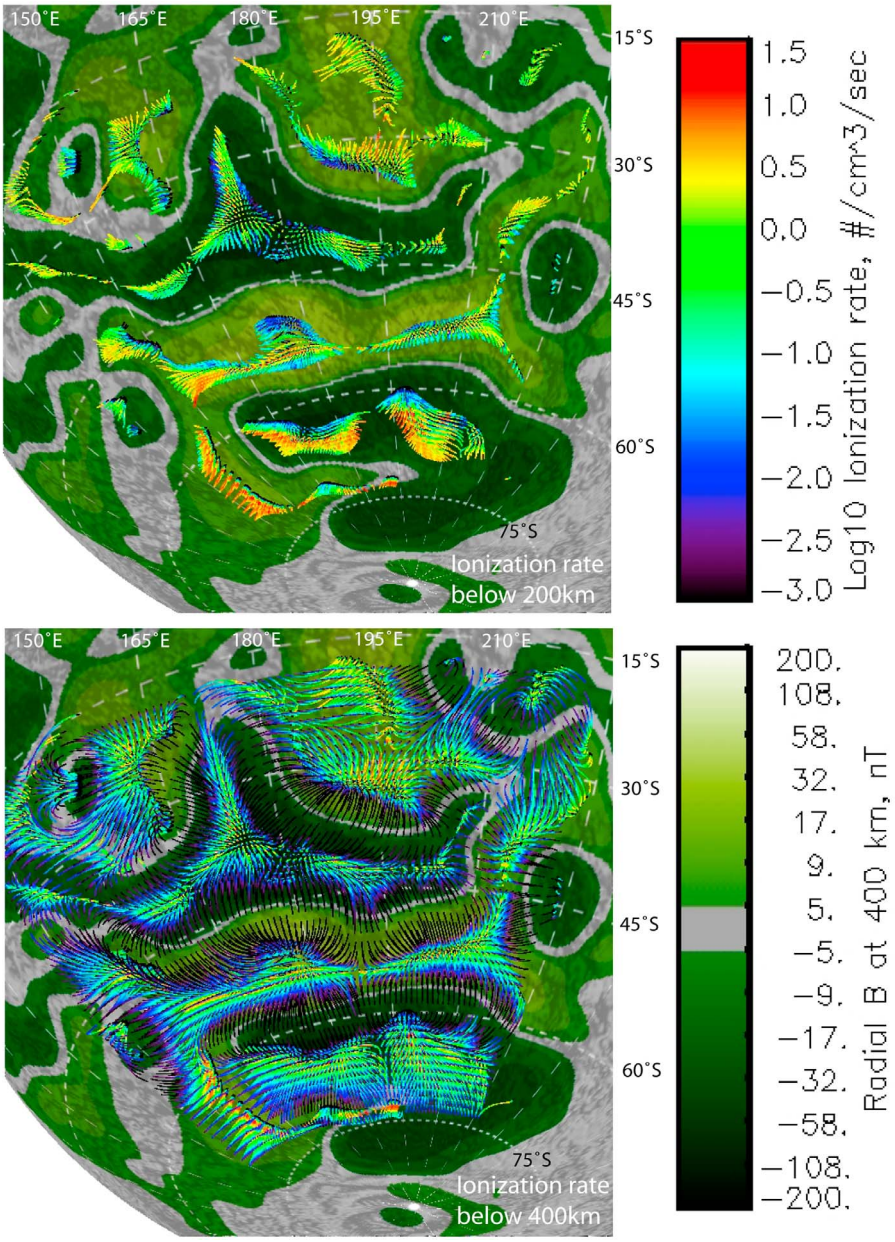

Figure 7. (top) Average predicted ionization rate in three dimensions traced from the middle of every 1° × 1° pixel at MGS spacecraft altitude down to 80 km. (bottom) The dark and light green colors on the globe represent the radial components of the crustal magnetic field measured by MGS at 400 km. For clarity, Figure 7 (top) shows only those points below 200 km altitude, while Figure 7 (bottom) shows all points.

relatively sparse below ~350 km. Therefore, despite validation by comparison with these data points, the modeled path of the field lines will not in reality be exactly like that shown in the figures. This is particularly true below ~200 km where shorter wavelength features will appear in the real magnetic field, thereby somewhat narrowing or widening as well as splitting, the various "lanes" of ionization compared to those shown in the figures, depending on the details of the true low-altitude crustal fields. So, while the patterns shown in this paper are the best estimates available and while the general large-scale patterns will not change with better data, the small-scale details may be different.

[44] However, as imperfect as these predictions may be, we believe they are useful for several reasons. First, this is the first prediction of Martian nightside ionization rate that takes into account the measured PADs and energy spectra of the precipitating electrons, as well as realistic magnetic mirroring by the crustal fields. Second, the three-dimensional ionization patterns in the paper should help other researchers visualize the complex geometries and the interplay between those geometries, the precipitating fluxes and the resulting ionization patterns. Third, these model predictions inform our expectations for the ionospheric data that the NASA MAVEN Mars Scout mission will return,

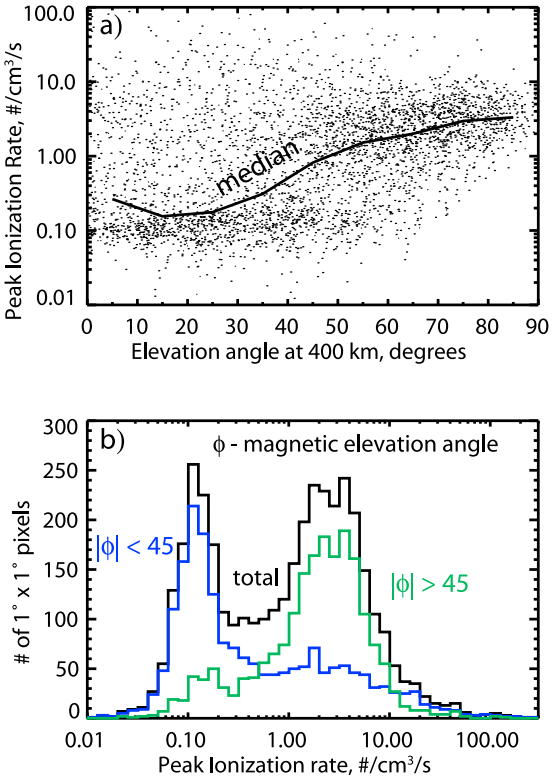

Figure 8. (a) Peak ionization rate as a function of elevation angle (all 4000 individual points and their medians in each 10° elevation angle bin). (b) Histogram of peak ionization in each pixel (black) plus separate histograms for measurements where the magnetic elevation angle is less than/greater than 45°.

starting in late 2014. Fourth, this ionization is the source of plasma that drives the rich and unique ionospheric electrodynamics of the Martian nightside, which we will now briefly discuss.

4.2. Consequences of the Ionization

[45] Electron impact ionization is an important source of plasma in topologically accessible regions of the Martian nightside upper atmosphere and therefore a primary driver of the undoubtedly rich electrodynamics to be found there, particularly in the area of strong crustal magnetic fields examined in this paper. In particular, we expect complex current systems to form where the combination of collisions and electromagnetic forces causes electrons and ions to drift in different directions [e.g., *Heelis*, 2004; *Fillingim et al.*, 2010]. Above the exobase (~200 km) we expect magnetic field curvature and gradient drifts [e.g., *Parks*, 2004] to cause differential motion between electrons and ions akin to the Earth's ring current, as well as acceleration by parallel electric fields [*Dubinin et al.*, 2008a; *Brain et al.*, 2006].

[46] At and below the exobase there is an important interplay between plasma density, neutral density and magnetic field that results in the so-called ionospheric dynamo region [e.g., *Heelis*, 2004]. Above the altitude at which the ion gyrofrequency and ion-neutral collision frequency are equal, the dynamics of any extant plasma are dominated by magnetic effects. In this region, perpendicular electric fields cause both electrons and ions to drift in same direction, resulting in zero net current. Below the altitude at which the electron gyrofrequency and electron-neutral collision frequency are equal, electrons' and ions' dynamics are controlled by collisions, also resulting in zero net current. However, in between these two altitudes (i.e., the dynamo region), ions are collisionally coupled to the atmosphere and will move in the direction of an applied force (e.g., neutral wind) while electrons are magnetized and will move in a direction perpendicular to both the applied force and the magnetic field. The resulting currents can vary enormously in both direction and magnitude depending upon neutral wind velocities and crustal magnetic field strengths and geometries [*Fillingim et al.*, 2010]. Figure 9 shows the altitude variation of the dynamo region in the vicinity of strong crustal fields, relative to a typical ionospheric profile. The degree of altitude overlap between the dynamo region and the vicinity

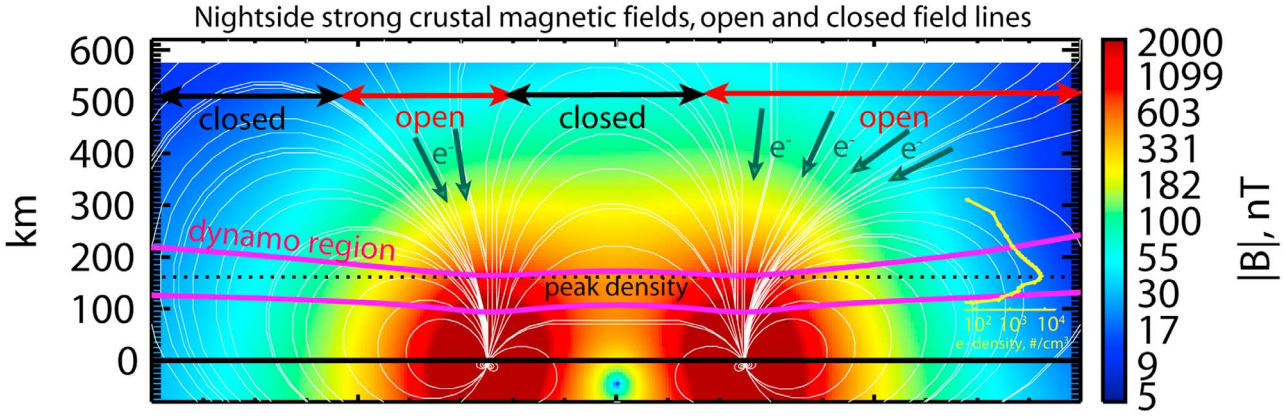

Figure 9. Martian ionospheric dynamo region superimposed on a typical strong crustal magnetic field morphology. The bottom and top of the dynamo region are defined as the altitudes at which the ratio of electron and ion gyrofrequencies to collision frequencies equal unity, respectively. Paths for solar wind electrons to precipitate into the atmosphere are shown with green arrows. A typical MarMCET nightside electron density profile is shown in yellow on the right-hand side.

of the ionospheric peak determines how much plasma is available to drive currents.

[47] Adding to this complexity is the fact that the resulting currents will produce magnetic fields that will themselves alter the magnetic geometry, which will alter those same currents, and so on self consistently [*Withers et al.*, 2005]. We must also consider day-night plasma transport [*Fränz et al.*, 2010] and parallel electric fields [*Dubinin et al.*, 2008a], both of which further complicate the electrodynamic picture. Finally, we have no in situ measurements of electron density below 270 km, no neutral wind measurements, no nightside electron temperature or species-specific neutral density measurements, no electric field measurements and no nightside thermal ion measurements. The result is that we currently have very little understanding of nightside electrodynamics. However, since electron impact ionization is the primary source of plasma on the nightside, the three-dimensional patterns of ionization rates explored in this paper are an important piece of the foundation upon which to build our understanding.

4.3. Looking Forward

[48] In future work, we intend to use MarMCET to build large sets of lookup tables of ionization rate profiles corresponding to different local times, seasons and crustal magnetic field strengths. These tables can, with interpolation, be used by Mars global plasma models, global circulation models and small-scale electrodynamic models to rapidly calculate three-dimensional patterns of electron impact ionization. We strongly encourage recent theoretical efforts to self consistently model these complex electrodynamics and we look forward hopefully to the wealth of new atmospheric and electrodynamic data in late 2014 promised by the upcoming MAVEN Mars Scout mission.

[49] **Acknowledgments.** We would like to thank François Forget and the LMD group in Paris for providing the Mars Climate Database. This work was supported by the NASA Mars Fundamental Research Program grant NNX09AD43G and by Mars Data Analysis Program grants NNX08AK94G and NNX11AI87G.

[50] Philippa Browning thanks the reviewers for their assistance in evaluating this paper.

References

Angelats i Coll, M., F. Forget, M. A. López-Valverde, P. L. Read, and S. Lewis (2004), Upper atmosphere of Mars up to 120 km: Mars Global Surveyor data analysis with the LMD general circulation model, *J. Geophys. Res.*, *109*, E01011, doi:10.1029/2003JE002163.

Arkani-Hamed, J. (2002), An improved 50-degree spherical harmonic model of the magnetic field of Mars derived from both high-altitude and low-altitude data, *J. Geophys. Res.*, *107*(E10), 5083, doi:10.1029/2001JE001835.

Barabash, S., et al. (2007), The Analyzer of Space Plasmas and Energetic Atoms (ASPERA-3) for the Mars Express mission, *Space Sci. Rev.*, *126*, 113–164, doi:10.1007/s11214-006-9124-8.

Bougher, S. W., S. Engle, R. G. Roble, and B. Foster (1999), Comparative terrestrial planet thermospheres: 2. Solar cycle variation of global structure and winds at equinox, *J. Geophys. Res.*, *104*, 16,591–16,611, doi:10.1029/1998JE001019.

Brain, D. A. (2006), Mars Global Surveyor measurements of the Martian solar wind interaction, *Space Sci. Rev.*, *126*, 77–112.

Brain, D. A., J. S. Halekas, L. M. Peticolas, R. P. Lin, J. G. Luhmann, D. L. Mitchell, G. T. Delory, S. W. Bougher, M. H. Acuña, and H. Rème (2006), On the origin of aurorae on Mars, *Geophys. Res. Lett.*, *33*, L01201, doi:10.1029/2005GL024782.

Brain, D. A., R. J. Lillis, D. L. Mitchell, J. S. Halekas, and R. P. Lin (2007), Electron pitch angle distributions as indicators of magnetic field topology near Mars, *J. Geophys. Res.*, *112*, A09201, doi:10.1029/2007JA012435.

Cain, J. C., B. B. Ferguson, and D. Mozoni (2003), An $n = 90$ internal potential function of the Martian crustal magnetic field, *J. Geophys. Res.*, *108*(E2), 5008, doi:10.1029/2000JE001487.

Chapman, S. (1931a), The absorption and dissociative or ionizing effect of monochromatic radiation in an atmosphere on a rotating Earth, *Proc. Phys. Soc. London*, *43*, 26–45, doi:10.1088/0959-5309/43/1/305.

Chapman, S. (1931b), The absorption and dissociative or ionizing effect of monochromatic radiation in an atmosphere on a rotating Earth, part II: Grazing incidence, *Proc. Phys. Soc. London*, *43*, 483–501, doi:10.1088/0959-5309/43/5/302.

Chen, R. H., T. E. Cravens, and A. F. Nagy (1978), The Martian ionosphere in light of the Viking observations, *J. Geophys. Res.*, *83*, 3871–3876, doi:10.1029/JA083iA08p03871.

Dubinin, E., G. Chanteur, M. Fraenz, and J. Wocha (2008a), Field-aligned currents and parallel electric field potential drops at Mars: Scaling from the Earth's aurora, *Planet. Space Sci.*, *56*, 868–872, doi:10.1016/j.pss.2007.01.019.

Dubinin, E., M. Fraenz, J. Woch, J. D. Winnigham, R. Frahm, R. Lundin, and S. Barabash (2008b), Suprathermal electron fluxes on the nightside of Mars: ASPERA-3 observations, *Planet. Space Sci.*, *56*, 846–851, doi:10.1016/j.pss.2007.12.010.

Dubinin, E., M. Fraenz, J. Woch, S. Barabash, and R. Lundin (2009), Long-lived auroral structures and atmospheric losses through auroral flux tubes on Mars, *Geophys. Res. Lett.*, *36*, L08108, doi:10.1029/2009GL038209.

Eliasson, L., M. Andre, R. Lundin, R. Pottelette, G. Marklund, and G. Holmgren (1996), Observations of electron conics by the Viking satellite, *J. Geophys. Res.*, *101*, 13,225–13,238, doi:10.1029/95JA02386.

Espley, J. R., J. E. C. Connerney, and R. J. Lillis (2008), Effects of high energy astrophysical events on the Martian atmosphere, paper presented at Third International Conference on the Mars Atmosphere: Modeling and Observations, Lunar and Planet. Inst., Williamsburg, Va.

Ferguson, B. B., J. C. Cain, D. H. Crider, D. A. Brain, and E. M. Harnett (2005), External fields on the nightside of Mars at Mars Global Surveyor mapping altitudes, *Geophys. Res. Lett.*, *32*, L16105, doi:10.1029/2004GL021964.

Fillingim, M. O., L. M. Peticolas, R. J. Lillis, D. A. Brain, J. S. Halekas, D. L. Mitchell, R. P. Lin, D. Lummerzheim, S. W. Bougher, and D. L. Kirchner (2007), Model calculations of electron precipitation induced ionization patches on the nightside of Mars, *Geophys. Res. Lett.*, *34*, L12101, doi:10.1029/2007GL029986.

Fillingim, M. O., L. M. Peticolas, R. J. Lillis, D. A. Brain, J. S. Halekas, D. Lummerzheim, and S. W. Bougher (2010), Localized ionization patches in the nighttime ionosphere of Mars and their electrodynamic consequences, *Icarus*, *206*, 112–119, doi:10.1016/j.icarus.2009.03.005.

Forget, F., F. Hourdin, R. Fournier, C. Hourdin, O. Talagrand, M. Collins, S. R. Lewis, P. L. Read, and J.-P. Huot (1999), Improved general circulation models of the Martian atmosphere from the surface to above 80 km, *J. Geophys. Res.*, *104*, 24,155–24,175, doi:10.1029/1999JE001025.

Forget, F., F. Montmessin, J.-L. Bertaux, F. González-Galindo, S. Lebonnois, E. Quémerais, A. Reberac, E. Dimarellis, and M. A. López-Valverde (2009), Density and temperatures of the upper Martian atmosphere measured by stellar occultations with Mars Express SPICAM, *J. Geophys. Res.*, *114*, E01004, doi:10.1029/2008JE003086.

Fox, J. L., J. F. Brannon, and H. S. Porter (1993), Upper limits to the nightside ionosphere of Mars, *Geophys. Res. Lett.*, *20*, 1339–1342, doi:10.1029/93GL01349.

Fränz, M., E. Dubinin, E. Nielsen, J. Woch, S. Barabash, R. Lundin, and A. Fedorov (2010), Transterminator ion flow in the Martian ionosphere, *Planet. Space Sci.*, *58*, 1442–1454, doi:10.1016/j.pss.2010.06.009.

Gurnett, D. A., et al. (2005), Radar soundings of the ionosphere of Mars, *Science*, *310*, 1929–1933, doi:10.1126/science.1121868.

Gurnett, D. A., et al. (2008), An overview of radar soundings of the Martian ionosphere from the Mars Express spacecraft, *Adv. Space Res.*, *41*, 1335–1346, doi:10.1016/j.asr.2007.01.062.

Haider, S. A. (1997), Chemistry of the nightside ionosphere of Mars, *J. Geophys. Res.*, *102*, 407–416, doi:10.1029/96JA02353.

Haider, S. A., J. Kim, A. F. Nagy, C. N. Keller, M. I. Verigin, K. I. Gringauz, N. M. Shutte, K. Szego, and P. Kiraly (1992), Calculated ionization rates, ion densities, and airglow emission rates due to precipitating electrons in the nightside ionosphere of Mars, *J. Geophys. Res.*, *97*, 10,637–10,641, doi:10.1029/92JA00317.

Haider, S. A., S. P. Seth, E. Kallio, and K. I. Oyama (2002), Solar EUV and electron-proton-hydrogen atom-produced ionosphere on Mars: Comparative studies of particle fluxes and ion production rates due to different sources, *Icarus*, *159*, 18–30, doi:10.1006/icar.2002.6919.

Haider, S. A., V. Singh, V. R. Choksi, W. C. Maguire, and M. I. Verigin (2007), Calculated densities of H_3O^+ $(H^2O)_n$, NO_2^- $(H_2O)_n$, CO_3^- $(H_2O)_n$ and electron in the nighttime ionosphere of Mars: Impact of solar wind

electron and galactic cosmic rays, *J. Geophys. Res.*, *112*, A12309, doi:10.1029/2007JA012530.
Halekas, J. S., D. A. Brain, R. J. Lillis, M. O. Fillingim, D. L. Mitchell, and R. P. Lin (2006), Current sheets at low altitudes in the Martian magnetotail, *Geophys. Res. Lett.*, *33*, L13101, doi:10.1029/2006GL026229.
Halekas, J. S., D. A. Brain, R. P. Lin, J. G. Luhmann, and D. L. Mitchell (2008), Distribution and variability of accelerated electrons at Mars, *Adv. Space Res.*, *41*, 1347–1352.
Hanson, W. B., and G. P. Mantas (1988), Viking electron temperature measurements: Evidence for a magnetic field in the Martian atmosphere, *J. Geophys. Res.*, *93*, 7538–7544, doi:10.1029/JA093iA07p07538.
Heelis, R. A. (2004), Electrodynamics in the low and middle latitude ionosphere: A tutorial, *J. Atmos. Sol. Terr. Phys.*, *66*, 825–838, doi:10.1016/j.jastp.2004.01.034.
Inan, U. S., N. G. Lehtinen, R. C. Moore, K. Hurley, S. Boggs, D. M. Smith, and G. J. Fishman (2007), Massive disturbance of the daytime lower ionosphere by the giant γ-ray flare from magnetar SGR 1806-20, *Geophys. Res. Lett.*, *34*, L08103, doi:10.1029/2006GL029145.
Langlais, B., M. E. Purucker, and M. Mandea (2004), Crustal magnetic field of Mars, *J. Geophys. Res.*, *109*, E02008, doi:10.1029/2003JE002048.
Leblanc, F., J. G. Luhmann, R. E. Johnson, and E. Chassefiere (2002), Some expected impacts of a solar energetic particle event at Mars, *J. Geophys. Res.*, *107*(A5), 1058, doi:10.1029/2001JA900178.
Leblanc, F., O. Witasse, J. Winningham, D. Brain, J. Lilensten, P.-L. Blelly, R. A. Frahm, J. S. Halekas, and J. L. Bertaux (2006), Origins of the Martian aurora observed by Spectroscopy for Investigation of Characteristics of the Atmosphere of Mars (SPICAM) on board Mars Express, *J. Geophys. Res.*, *111*, A09313, doi:10.1029/2006JA011763.
Leblanc, F., et al. (2008), Observations of aurorae by SPICAM ultraviolet spectrograph on board Mars Express: Simultaneous ASPERA-3 and MARSIS measurements, *J. Geophys. Res.*, *113*, A08311, doi:10.1029/2008JA013033.
Lillis, R. J., D. L. Mitchell, R. P. Lin, J. E. P. Connerney, and M. H. Acuña (2004), Mapping crustal magnetic fields at Mars using electron reflectometry, *Geophys. Res. Lett.*, *31*, L15702, doi:10.1029/2004GL020189.
Lillis, R. J., D. L. Mitchell, R. P. Lin, and M. H. Acuña (2008), Electron reflectometry in the Martian atmosphere, *Icarus*, *194*, 544–561, doi:10.1016/j.icarus.2007.09.030.
Lillis, R. J., M. O. Fillingim, L. M. Peticolas, D. A. Brain, R. P. Lin, and S. W. Bougher (2009), The nightside ionosphere of Mars: Modeling the effects of crustal magnetic fields and electron pitch angle distributions on electron impact ionization, *J. Geophys. Res.*, *114*, E11009, doi:10.1029/2009JE003379.
Lillis, R. J., M. E. Purucker, J. S. Halekas, K. L. Louzada, S. T. Stewart-Mukhopadhyay, M. Manga, and H. V. Frey (2010a), Study of impact demagnetization at Mars using Monte Carlo modeling and multiple altitude data, *J. Geophys. Res.*, *115*, E07007, doi:10.1029/2009JE003556.
Lillis, R. J., D. A. Brain, S. L. England, P. Withers, M. O. Fillingim, and A. Safaeinili (2010b), Total electron content in the Mars ionosphere: Temporal studies and dependence on solar EUV flux, *J. Geophys. Res.*, *115*, A11314, doi:10.1029/2010JA015698.
Luhmann, J. G., C. Zeitlin, R. Turner, D. A. Brain, G. Delory, J. G. Lyon, and W. Boynton (2007), Solar energetic particles in near-Mars space, *J. Geophys. Res.*, *112*, E10001, doi:10.1029/2006JE002886.
Millour, E., et al. (2008), The latest (version 4.3) Mars Climate Database, *LPI Contrib.*, *1447*, 9029.
Mitchell, D. L., R. P. Lin, C. Mazelle, H. Rème, P. A. Cloutier, J. E. P. Connerney, M. H. Acuña, and N. F. Ness (2001), Probing Mars' crustal magnetic field and ionosphere with the MGS electron reflectometer, *J. Geophys. Res.*, *106*, 23,419–23,427, doi:10.1029/2000JE001435.
Nagy, A. F., et al. (2004), The plasma environment of Mars, *Space Sci. Rev.*, *111*, 33–114.
Němec, F., D. D. Morgan, D. A. Gurnett, and F. Duru (2010), Nightside ionosphere of Mars: Radar soundings by the Mars Express spacecraft, *J. Geophys. Res.*, *115*, E12009, doi:10.1029/2010JE003663.
Nier, A. O., and M. B. McElroy (1977), Composition and structure of Mars' upper atmosphere: Results from the neutral mass spectrometers on Viking 1 and 2, *J. Geophys. Res.*, *82*, 4341–4349, doi:10.1029/JS082i028p04341.
Parks, G. (2004), *Physics of Space Plasmas*, Westview, Boulder, Colo.
Purucker, M. E. (2008), A global model of the internal magnetic field of the Moon based on Lunar Prospector magnetometer observations, *Icarus*, *197*, 19–23, doi:10.1016/j.icarus.2008.03.016.
Safaeinili, A., W. Kofman, J. Mouginot, Y. Gim, A. Herique, A. B. Ivanov, J. J. Plaut, and G. Picardi (2007), Estimation of the total electron content of the Martian ionosphere using radar sounder surface echoes, *Geophys. Res. Lett.*, *34*, L23204, doi:10.1029/2007GL032154.
Schunk, R. W., and A. F. Nagy (2000), *Ionospheres: Physics, Plasma Physics, and Chemistry*, Cambridge Univ. Press, New York, doi:10.1017/CBO9780511551772.
Seth, S. P., S. A. Haider, and K. I. Oyama (2002), The photoelectron flux and nightglow emissions of 5577 and 6300 Å due to solar wind electron precipitation in Martian atmosphere, *J. Geophys. Res.*, *107*(A10), 1324, doi:10.1029/2001JA000261.
Sheehan, C. H., and J.-P. St.-Maurice (2004), Dissociative recombination of N_2^+, O_2^+, and NO^+: Rate coefficients for ground state and vibrationally excited ions, *J. Geophys. Res.*, *109*, A03302, doi:10.1029/2003JA010132.
Tyler, G. L., G. Balmino, D. P. Hinson, W. L. Sjogren, D. E. Smith, R. A. Simpson, S. W. Asmar, P. Priest, and J. D. Twicken (2001), Radio science observations with Mars Global Surveyor: Orbit insertion through one Mars year in mapping orbit, *J. Geophys. Res.*, *106*, 23,327–23,348, doi:10.1029/2000JE001348.
Ulusen, D., and I. R. Linscott (2008), Low-energy electron current in the Martian tail due to reconnection of draped interplanetary magnetic field and crustal magnetic fields, *J. Geophys. Res.*, *113*, E06001, doi:10.1029/2007JE002916.
Ulusen, D., D. A. Brain, and D. L. Mitchell (2011), Observation of conical electron distributions over Martian crustal magnetic fields, *J. Geophys. Res.*, *116*, A07214, doi:10.1029/2010JA016217.
Verigin, M. I., K. I. Gringauz, N. M. Shutte, S. A. Haider, K. Szego, P. Kiraly, A. F. Nagy, and T. I. Gombosi (1991), On the possible source of the ionization in the nighttime Martian ionosphere: 1. Phobos 2 HARP electron spectrometer measurements, *J. Geophys. Res.*, *96*, 19,307–19,313, doi:10.1029/91JA00924.
Wedlund, C. S., G. Gronoff, J. Lilensten, H. Ménager, and M. Barthélemy (2011), Comprehensive calculation of the energy per ion pair or *W* values for five major planetary upper atmospheres, *Ann. Geophys.*, *29*, 187–195, doi:10.5194/angeo-29-187-2011.
Whaler, K. A., and M. E. Purucker (2005), A spatially continuous magnetization model for Mars, *J. Geophys. Res.*, *110*, E09001, doi:10.1029/2004JE002393.
Withers, P. (2006), Mars Global Surveyor and Mars Odyssey accelerometer observations of the Martian upper atmosphere during aerobraking, *Geophys. Res. Lett.*, *33*, L02201, doi:10.1029/2005GL024447.
Withers, P. (2009), A review of variability in the dayside ionosphere of Mars, *Adv. Space Res.*, *44*, 277–307, doi:10.1016/j.asr.2009.04.027.
Withers, P., S. W. Bougher, and G. M. Keating (2003), The effects of topographically controlled thermal tides in the Martian upper atmosphere as seen by the MGS accelerometer, *Icarus*, *164*, 14–32, doi:10.1016/S0019-1035(03)00135-0.
Withers, P., M. Mendillo, H. Rishbeth, D. P. Hinson, and A. J. Arkani-Hamed (2005), Ionospheric characteristics above Martian crustal magnetic anomalies, *Geophys. Res. Lett.*, *32*, L16204, doi:10.1029/2005GL023483.
Zhang, M. H. G., J. G. Luhmann, and A. J. Kliore (1990), An observational study of the nightside ionospheres of Mars and Venus with radio occultation methods, *J. Geophys. Res.*, *95*, 17,095–17,102, doi:10.1029/JA095iA10p17095.

D. A. Brain, Laboratory for Atmospheric and Space Physics, University of Colorado at Boulder, 1234 Innovation Dr., Boulder, CO 80303, USA.
M. O. Fillingim and R. J. Lillis, Space Sciences Laboratory, University of California, 7 Gauss Way, Berkeley, CA 94720, USA. (rlillis@ssl.berkeley.edu)